



42nd European Rotorcraft Forum  
Lille, France, 5–8 September, 2016  
Paper 56

## AERODYNAMIC STUDY OF TILTROTOR BLADES

**Antonio Jimenez Garcia**  
a.jimenez-garcia.1@research.gla.ac.uk  
CFD Laboratory, School of Engineering  
James Watt South Building  
University of Glasgow, G12 8QQ, U.K.

**George N. Barakos**  
George.Barakos@glasgow.ac.uk  
CFD Laboratory, School of Engineering  
James Watt South Building  
University of Glasgow, G12 8QQ, U.K.

### Abstract

This paper presents performance analysis of the full-scale XV-15 rotor with high-fidelity computational fluids dynamics. A comparison of computed rotor loads with experiments was carried out, where CFD results predicted the FoM within 1%. The method was also able to capture the differences in performance between hover and propeller modes. The effect of flow transition was also assessed, showing the capability of modern CFD methods. The transition onset and the distribution of the skin friction were well predicted, and found to have a mild effect on the overall figure of merit. The overall agreement with the experimental data and theory for the considered case demonstrates the capability of the present CFD method to accurately predict tiltrotor flows.

### 1 INTRODUCTION

Tiltrotor is a new type of flying vehicle that combines VTOL (vertical take-off/landing) capability with high speed cruise. For the first time, this technology was successfully demonstrated with the Bell XV-3 in 1955 [1]. In the late 1960s and early 1970s, a major program was jointly launched at the NASA Ames Research Center and Bell Helicopters, to develop a new tiltrotor named XV-15. The results of that effort supported the development of new generation of tiltrotors like the Bell-Boeing V-22 Osprey [2, 3] and the AW609 [4].

Very little wind tunnel data is available for model and full-scale tiltrotors. At the early stage of the XV-15 program, the NASA 40-by-80-Foot Wind Tunnel

was used to measure integrated rotor loads in helicopter [5], aeroplane and transition-corridor modes [6]. However, force and moment measurements did not exclude the contribution from the airframe. The NASA-Ames Outdoor Aeronautical Research Facility (OARF) was also extensively used by Felker *et al.* [7] with the XV-15 rotor and Bartie *et al.* [8] with the XV-15 Advanced Technology Blade (ATB). The hover and forward flight tests began in the late 90s with the work of Light [9] in the 80-ft by 120-ft wind tunnel at NASA Ames, but only few conditions were tested. To fill this gap, Betzina [10] in 2002 undertook an extensive campaign of experiments on the full-scale XV-15 rotor, where the experiments were corrected for hub and tare effects.

For all sets of experiments cited, neither sur-

---

Copyright Statement© The authors confirm that they, and/or their company or organisation, hold copyright on all of the original material included in this paper. The authors also confirm that they have obtained permission, from the copyright holder of any third party material included in this paper, to publish it as part of their paper. The authors confirm that they give permission, or have obtained permission from the copyright holder of this paper, for the publication and distribution of this paper as part of the ERF2016 proceedings or as individual offprints from the proceedings and for inclusion in a freely accessible web-based repository.

face pressure nor skin friction coefficients were measured. In this regard, Wadcook *et al.* [11] measured skin friction coefficients on a hovering full-scale XV-15 tiltrotor in the 80-ft by 120-ft wind tunnel at NASA Ames. At low thrust, a region of laminar flow was encountered over a significant fraction of the blade chord, while at high disc loading conditions, the laminar to turbulent transition region on the upper blade surface moved towards the blade leading edge, with fully turbulent boundary layer encountered outboard. This set of experiments could be employed to validate and improve transitional models for tiltrotors.

Concerning numerical simulations of tiltrotor blades, Kaul *et al.* [12, 13] studied the effect of inflow boundary conditions and turbulent models on the hovering XV-15 rotor blade, using the OVERFLOW2 CFD solver. Results with the Spalart-Allmaras model [14] with the Detached Eddy Simulation formulation, revealed lack of agreement with the experiments of Wadcook *et al.* [11] in the laminar-turbulent transitional region. Likewise, Yoon *et al.* [15] investigated the effect of the employed turbulence model on the hovering performance and skin friction coefficients of the XV-15 rotor blade at a collective of  $10^\circ$ . It was found that the  $k - \omega$  SST-DDES turbulence model predicted the figure of merit closer to experiment than the SA-DDES one-equation model. However, minimal differences between these fully-turbulent models were observed in the predictions of skin friction coefficient, which did not reproduce well the flowfield encountered in the experiment [11]. Sheng *et al.* [16] used the U<sup>2</sup>NCLE and Helios CFD solvers to assess the effect of transition models in predicting the hover figure of merit on the XV-15 blade. Despite the use of a massive grid of 294 million cells for the whole rotor, results at  $10^\circ$  collective showed an over-predicted FoM with a discrepancy of more than 3%. It was shown that the transitional flow modelling did not have a significant impact on the predicted FoM mainly due to the small laminar-turbulent transition region encountered on the XV-15 blades. A detailed performance analysis of the hover and propeller modes of the XV-15 blades were performed by Gates [17] using the HMB CFD solver. Good agreement with published experimental data was reported, even though a medium grid size (9.6 million cells per blade) was employed for computations. Furthermore, the effect of the hub spinner on the propeller performance at moderate advance ratios was highlighted.

Further studies have also been published for the V-22 tiltrotor using numerical simulations. The drag polar of the V-22 aircraft has been measured in the 20×20ft Boeing wind tunnel [18] and the results were compared against CFD predictions of the FUN3D and OVERFLOW CFD codes. Neither CFD nor experiments considered the effect of the rotors. The experiments considered a model of the V-22 of 0.15 scale and provided integrated lift, drag and moment data. In general, the authors state that good agreement between the CFD and experiments was obtained even if further studies were recommended to ensure that mesh independent results can be obtained.

In this work, we present an aerodynamic study of the XV-15 tiltrotor blades with high-fidelity computational fluid dynamics. The aim is to assess the level of accuracy of the present CFD method in predicting the figure of merit for a hover case. This is addressed by comparing with experimental data available in the literature [7, 9, 10]. To reduce the computational cost, we solved the hover flow by casting the equations as a steady-state problem in a noninertial reference frame. Results are presented for a range of design points, which includes medium and high thrust hover conditions. The second objective is to investigate the impact of a fully-turbulent  $k - \omega$  SST and transitional  $k - \omega$  SST- $\gamma$  models on the predicted figure of merit at collective angles of  $3^\circ$  and  $10^\circ$ . Moreover, the ability of those models in predicting the experimental skin friction distribution [11] on the blade surface is also discussed.

## 2 CFD METHOD

### 2.1 HMB Solver

The Helicopter Multi-Block (HMB) [19, 20, 21] code is used as the CFD solver for the present work. It solves the Unsteady Reynolds Averaged Navier-Stokes (URANS) equations in integral form using the Arbitrary Lagrangian Eulerian (ALE) formulation for time-dependent domains, which may include moving boundaries. The Navier-Stokes equations are discretised using a cell-centred finite volume approach on a multi-block grid. The spatial discretisation of these equations leads to a set of ordinary differential equations in time,

$$(1) \quad \frac{d}{dt}(\mathbf{W}_{i,j,k} V_{i,j,k}) = -\mathbf{R}_{i,j,k}(\mathbf{W})$$

where  $i, j, k$  represent the cell index,  $\mathbf{W}$  and  $\mathbf{R}$  are the vector of conservative flow variables and flux residual respectively, and  $V_{i,j,k}$  is the volume of the cell  $i, j, k$ . To evaluate the convective fluxes, Osher [22] and Roe [23] approximate Riemann solvers are used in HMB, while the viscous terms are discretised using a second order central differencing spatial discretisation. The Monotone Upstream-centred Schemes for Conservation Laws, which is referred to in the literature as the MUSCL approach and developed by Leer [24], is used to provide third order accuracy in space. The HMB solver uses the alternative form of the Albada limiter [25] being activated in regions where a large gradients are encountered mainly due to shock waves, avoiding the non-physical spurious oscillations. An implicit dual-time stepping method is employed to performed the temporal integration, where the solution is marching in pseudo-time iterations to achieve fast convergence, which is solved using a first-order backward difference. The linearised system of equations is solved using the Generalised Conjugate Gradient method with a Block Incomplete Lower-Upper (BILU) factorisation as a pre-conditioner [26]. To allow an easy sharing of the calculation load for parallel job, a multi-block structured meshes are used. Overset grid and sliding plane methods are available in HMB [20, 27] to allow the relative motion between different components. Both methods have been widely employed for isolated rotor blades, such as the UH-60A and S-76 by Dehaeze *et al.* [28] and Jimenez *et al.* [29], respectively, and complete helicopter configurations [20]. For the present work, an overset grid method is employed to explore its capabilities with tiltrotor configurations.

## 2.2 Turbulence and Transition Models

Various turbulence models are available in HMB, including several one-equation, two-equation, three-equation, and four-equation turbulence models. Furthermore, Large-Eddy Simulation (LES), Detached-Eddy Simulation (DES) and Delay-Detached-Eddy Simulation (DDES) are also available. For this study, two and three equations models were employed using the fully-turbulent  $k - \omega$  SST and the transitional model  $k - \omega$  SST- $\gamma$  both from Menter [30, 31]. It is well known that the fully-turbulent  $k - \omega$  SST model predicts the transition onset further upstream than nature, being needed the use of transitional models. In this regard, Menter *et al.* [32] developed a model for the

prediction of laminar-turbulent transitional flows, involving two transport equations for the intermittency factor  $\gamma$  and the momentum thickness Reynolds number  $Re_\theta$ . The intermittency factor  $\gamma$  is used to trigger and control the transition onset location, and it varies between 0 (laminar flow) to 1 (fully-turbulent flow). In 2015, a new one-equation local correlation-based transition model  $\gamma$  was proposed by Menter *et al.* [31], where the  $Re_\theta$  equation was avoided. The form of the transport equation for the intermittency factor  $\gamma$  reads as:

$$(2) \quad \frac{\partial(\rho\gamma)}{\partial t} + \frac{\partial(\rho U_j \gamma)}{\partial x_j} = P_\gamma - E_\gamma + \frac{\partial}{\partial x_j} \left[ \left( \mu + \frac{\mu_t}{\sigma_\gamma} \right) \frac{\partial \gamma}{\partial x_j} \right]$$

where  $P_\gamma$  and  $E_\gamma$  represent the production and destruction sources, respectively. A more detailed description of the  $\gamma$  equation can be found in Menter *et al.* [31].

## 3 XV-15 ROTOR GEOMETRY

The three-bladed XV-15 rotor geometry was generated based on the full-scale wind tunnel model performed by Betzina in the NASA Ames 80- by 120-foot wind tunnel facility [10]. NACA 6-series five-digit aerofoil sections comprise the rotor blade, and its identity and radial location along the rotor blade is reported in Table 1.

The main geometric characteristics of the XV-15 rotor blades [10] are summarised in Table 2. It is interesting to note that unlike convectional helicopter blades, tiltrotor blades are characterised by high twist and solidity, along with a small rotor radius.

A detailed sketch of the XV-15 blade planform and the blade radial twist, and chord distributions is shown in Figure 1. The rotor blade chord is held constant, and extends at almost 80% of the rotor blade. The blade root, however, was not modelled due to the lack of information on the cuff geometry in the literature.

## 4 XV-15 ROTOR MESH

A mesh generated using the chimera technique was used for the aerodynamic study of the XV-15 rotor. It was composed by a Cartesian off-body mesh used as background, and a body-fitted mesh for the blade. The use of an overset grid method

allowed for the blade pitch angle to be changed by rotating the body-fitted mesh. Because the XV-15 rotor was numerically evaluated in hover and propeller modes (axial flight), only a third of the computational domain was meshed, assuming periodic conditions for the flowfield in the azimuthal direction (not applicable to stall condition). A view of the computational domain, along with the boundary conditions employed is given in Figure 2 (a). Farfield boundaries were extended to  $2R$  (above rotor) and  $4R$  (below rotor and in the radial direction) from the rotor plane, which assures an independent solution with the boundary conditions employed. Furthermore, an ideal rotor hub was modelled and approximated as a cylinder, extending from inflow to outflow with a radius of  $0.05R$ .

A C-topology was selected for the leading edge of the blade, while an H-topology was employed at the trailing edge. This configuration permits an optimal resolution of the boundary layer due to the orthogonality of the cells around the surface blade (Figure 2 (b)). The height of the first mesh layer above the blade surface was set to  $1.0 \cdot 10^{-5} c_{ref}$ , which leads to  $y^+$  less than 1.0 all over the blade. Considering the chordwise and spanwise directions of the blade, 264 and 132 mesh points were used, while the blunt trailing-edge was modelled with 42 mesh points.

To guarantee a mesh independent solution, two computational domains were built. Table 3 lists the grids used and shows the breakdown of cells per blade. The coarse and medium meshes have 6.2 and 9.6 million cells per blade (equivalent to 18.6 and 28.8 million cells for three blades), with the same grid resolution for the body-fitted mesh (3.6 million cells). The background mesh, however, was refined at the wake and near-body regions, increasing the grid size from 2.6 to 6 million cells.

## 5 TEST CONDITIONS

Table 4 summarises the conditions employed and computations performed in hover and propeller modes. For the hover mode, the tip Mach number was set to 0.69, and four blade collective angles were considered, corresponding to low, medium, and high disc loadings. The Reynolds number, based on the reference blade chord of 14 inches and on the tip speed, was  $4.95 \cdot 10^6$ . The cruise condition was modelled at 0 ft (ISA+0°), with a tip Mach number of 0.54 and advance ratio 0.337. The

Reynolds number for this case was  $4.50 \cdot 10^6$ , again based on the reference blade chord and rotor tip speed (with no account for the advance velocity).

All flow solutions were computed by solving the RANS equations, coupled with Menter's  $k - \omega$  SST turbulence model [30]. The flow equations were integrated with the implicit dual-time stepping method of HMB, using a pseudo-time Courant–Friedrichs–Lewy (CFL) equal to 4 for the helicopter mode computations, and equal to 2 for the aeroplane mode. Typically, 40,000 iterations were necessary to drop the residual by 6 orders of magnitude for the flow solutions.

## 6 RESULTS

### 6.1 Helicopter Mode

The effect of the mesh density on the figure of merit, and torque coefficient  $C_Q$  as functions of the thrust coefficient  $C_T$  are shown in Figure 3. Experimental data of the full-scale XV-15 rotor is also shown, carried out by Felker *et al.* [7] at OARF, and Light [9] and Betzina [10] at the NASA 80×120ft wind tunnel. The majority of works on performance analysis of rotor blades do not model the hub and root apparatus, mainly due to the complexity of mesh generation. In this regard, experiments were corrected for hub and apparatus tare effects. Vertical lines labelled as empty (4,574 kg) and maximum gross (6,000 kg) weight, define the hovering range of the XV-15 helicopter rotor [1]. Momentum-based estimates of the figure of merit are also included, and its expression is given in Equation 3, where an induced power factor  $k_i$  of 1.1 and overall profile drag coefficient  $C_{DO}$  of 0.01 were used. This theory, is limited to low and medium thrust, leading to a wrong trend of the power divergence at high thrust, mainly due to flow separation [33].

$$(3) \quad \text{FoM} = \frac{C_T^{3/2}}{\sqrt{2} \left( \sigma \frac{C_{DO}}{8} + k_i \frac{C_T^{3/2}}{\sqrt{2}} \right)}$$

Using the obtained CFD results, a polynomial fit was computed and shown with solid lines and squares (coarse grid) or triangles (medium grid). Considering the sets of experiments, good agreement was found between them, with a maximum discrepancy of 4.11% in the figure of merit. The reason for this disagreement (4 counts of FoM) may be partly due to the variations in experimental data between wind tunnel facilities. CFD results

present an excellent agreement with the test data of Betzina[10] for all blade collective angles. It is found that the effect of the grid size on the overall performance is negligible at low thrust, with a small influence at high thrust.

The comparison of the predicted and measured [7, 9, 10] peak figure of merit is reported in Table 5. Experiments performed by Felker show a higher Figure of Merit (2 counts) if compared with the Light and Betzina experiments. A large recirculation zone was reported in the 80×120 test section of NASA by Felker, which may be the reason of this disagreement. Predictions with the medium grid indicate good correlation with the experiments (0.91% respect to Betzina and Light, and 2.53% respect to Felker), which confirms the suitability of the present method for tiltrotor blade applications.

From a point of view of the turbulent model employed, it seems that the fully turbulent flow assumption is able to capture the trend of FoM and torque coefficient (Figure 3 (b)). Similar conclusions were drawn in previous work by Kaul *et al.* [12], Yoon *et al.* [15], and Sheng *et al.* [16], where fully turbulent flows were successfully employed. Comparison between predicted and measured [11] FoM at a collective pitch angle of 10° is reported in Table 6. Prediction with the medium grid indicates good correlation with the experiments (0.8 counts of FoM), which highlights the ability of this medium grid in accurately predicting the FoM with a modest CPU time.

### 6.1.1 Surface Pressure Predictions

Due to the lack of experimental surface pressure measurements, a comparison between HMB3 and CFD data published by Kaul *et al.* [13] using the OVERFLOW2 solver is shown in Figure 4. Three radial stations were considered ( $r/R=0.72$ , 0.83, and 0.94), and the collective pitch angle was 10°. The surface pressure coefficient is computed based on the local velocity at each radial station:

$$(4) \quad C_P = \frac{P - P_\infty}{1/2\rho_\infty(\Omega r)^2}.$$

CFD results using HMB3 correspond to the coarse grid (18.6 million cells for the three blades) where the  $k - \omega$  SST turbulence model [30] was employed, while Kaul's results were obtained with a grid size of 35 million cells using the Spalart-Allmaras turbulence model [14]. Despite that small

variation on the predicted peak  $C_P$ , a fair agreement is found for all radial stations. Regarding the radial stations  $r/R = 0.72$  and  $r/R = 0.83$ , it is clear that the suction peak does not exceed the critical  $C_P^*$  values (Eq. 5), while the most outboard section ( $r/R = 0.94$ ) reaches sonic conditions.

$$(5) \quad C_P^* = \frac{2}{\gamma(M_{\text{tip}} \frac{r}{R})^2} \left[ \left( \frac{2 + (\gamma - 1)(M_{\text{tip}} \frac{r}{R})^2}{\gamma + 1} \right)^{\frac{\gamma}{\gamma - 1}} - 1 \right].$$

### 6.1.2 Sectional Loads

Figure 5 shows the distribution of sectional thrust and torque coefficients along the rotor radius for collective pitch angles from 3° to 13°. The influence of the tip vortex on the tip region (from 92%R to 100% R) is visible in terms of loading and torque coefficients.

## 6.2 Aeroplane Mode

Like for hover simulations, only a third of the computational domain was meshed, modelling this case as steady-state problem with periodic conditions for the flow in the azimuthal direction. Simulations were performed for medium advance ratio  $\mu = 0.337$  at collective pitch angles of 26°, 27°, 28° and 28.8°, and tip Mach number of 0.54 (see Table 4). In aeroplane mode, the indicator of the rotor efficiency is the propeller propulsive efficiency, which is the ratio between the useful power output of the propeller and the absorbed power:

$$(6) \quad \eta = \frac{C_T V_\infty}{C_Q V_{\text{tip}}}.$$

Figure 6 compares the total load predictions with the available experimental data [5] (represented by square symbols), where the propeller efficiency  $\eta$  and torque coefficient are given as function of the thrust coefficient. The experimental data reported here, were performed on a propeller test rig in the NASA 40-by-80-Foot Wind Tunnel [5], and are the only available published data for the XV-15 in aeroplane mode. HMB3 results with the coarse grid show an under-predicted propulsive propeller efficiency for all thrust coefficient, with a maximum discrepancy of 4.5%. However, results with the medium grid provide a good agreement with the experimental data.

### 6.2.1 Surface Pressure Predictions

Figure 7 presents predicted pressure coefficient contours for the XV-15 upper blade at the computed advance ratio, where the  $C_P$  is computed based on the local velocity. Results at low thrust coefficient, confirm the idea that the inboard part of the rotor is over-loaded. As the collective pitch angle increased, contours of  $C_P$  at outboard part of the blade indicates a more uniform propeller load distributions.

### 6.2.2 Flowfield details

Flowfield visualisation of the rotor wake for the full-scale XV-15 rotor blade in propeller mode using the  $Q$  criterion [34] is given in Figure 8. Contours of surface pressure coefficient are also included. Despite that a coarse grid size was used as background (2.6 million cells), the wake development shows a well-preserved first and second passage of the vortex. Moreover, the interaction between blade and vortex typically encountered in hovering rotors is not presented here. In fact, the downstream convection of the rotor wake at  $M_\infty=0.182$ , results in a much less complex wake.

### 6.3 Effect of the Turbulence Model

In this study, the effect of the  $k - \omega$  SST- $\gamma$  transition model is investigated in predicting the figure of merit. The predicted skin friction coefficient is compared with measurements by Wadcock *et al.* [11]. Moreover, a comparison with the solution obtained with the fully-turbulent  $k - \omega$  SST model is presented. For this case, a matched grid was used, which has 10.2 million cells per blade.

Figures 9 and 10 show the computed skin friction coefficient  $C_f$  compared with the available experimental data of Wadcock *et al.* [35] for collective pitch angles of  $3^\circ$  and  $10^\circ$  at the radial stations  $r/R = 0.28, 0.50, 0.72, 0.83$  and  $0.94$ . At low disc loading (Figure 9), the experiment shows a natural transition for all stations at about 50% chord. It seems that the present transitional model is able to capture the onset and length of the natural transition with some discrepancies found at the inboard station  $r/R = 0.28$ . As expected, results obtained with the fully-turbulent model indicate lack of transition. Moreover, the values of skin friction coefficient are under and over-predicted in the laminar and turbulent flow regions. Considering the  $C_f$  at

collective pitch angle of  $10^\circ$  (Figure 10), the experimental  $C_f$  present a similar pattern as seen for the lower collective pitch angles. However, the onset of the natural transition is moved towards the leading edge, with a fully-turbulent flow region observed at the outboard station  $r/R = 0.94$ . Results corresponding to the transitional model accurately predicted the onset location and length of the transition. This physical phenomenon is not captured by the fully-turbulent solution. The surface skin friction coefficient of both turbulence models is shown in Figure 11, where the laminar-turbulent region can be only identified for the  $k - \omega$  SST- $\gamma$  model.

Once the distribution of skin friction coefficient was analysed, the impact of the turbulence model on the hover performance of the XV-15 blade was investigated. Table 7 reports the predicted  $C_T$ ,  $C_Q$ , and FoM using the fully-turbulent  $k - \omega$  SST and transitional model  $k - \omega$  SST- $\gamma$  at two disc loading conditions. It is shown that results are mildly sensitive to the turbulence model employed, with a higher figure of merit presented by the transitional model.

## 7 CONCLUSIONS

This paper demonstrated the capability of HMB3 to accurately predict tiltrotor flows. The full-scale XV-15 tiltrotor blades was considered for validation. The main conclusions are:

- The results obtained with CFD compare well with test data for the integrated blade load.
- The method was able to capture the performance in the different modes; hover and propeller.
- The transition onset and distribution of skin friction are well predicted and, for this case, were found to have a mild effect on the overall figure of merit.

## 8 ACKNOWLEDGMENTS

The use of the cluster Chadwick of the University of Liverpool is gratefully acknowledged. Some results were obtained using the EPSRC funded ARCHIE-WeSt High Performance Computer ([www.archie-west.ac.uk](http://www.archie-west.ac.uk)), EPSRC grant no. EP/K000586/1. Part of this work is funded under the HiperTilt Project of the UK Technology

Strategy Board (TSB) and Leonardo Helicopters under Contract Nr. 101370.

## 9 REFERENCES

- [1] Maisel, M. D., Giulianetti, D. J., and Dugan, D. C., "The History of the XV-15 Tilt Rotor Research Aircraft: From Concept to Flight," NASA SP-2000-4517, Feb. 2000.
- [2] Potsdam, M. A., Schaller, D. F., Rajagopalan, R. G., and Silva, M. J., "Tilt Rotor Aeromechanics Phenomena in Low Speed Flight," *Proceedings of the 4th Decennial Specialist's Conference on Aeromechanics*, AHS, San Francisco, CA, 2004, pp. 1–13.
- [3] Narducci, R., Jiang, F., Liu, J., and Clark, R., "CFD Modeling of Tiltrotor Shipboard Aerodynamics with Rotor Wake Interactions," *Proceedings of the 27th Applied Aerodynamics Conference*, AIAA, San Antonio, Texas, 2009, pp. 1–13.
- [4] Harris, J. C., Scheidler, P. F., Hopkins, R., and Fortenbaugh, R. L., "Initial Power-off Testing of the BA609 Tiltrotor," *Proceedings of the 66th Annual Forum*, AHS, Phoenix, Arizona, 2000, pp. 1–9.
- [5] "Advancement of Proprotor Technology, Task II - Wind-Tunnel Test Results," NASA CR-114363, Sept. 1971.
- [6] Weiberg, J. A. and Maisel, M. D., "Wind-Tunnel Tests of the XV-15 Tilt Rotor Aircraft," NASA TM-81177, April 1980.
- [7] Felker, F. F., Betzina, M. D., and Signor, D. B., "Performance and Loads Data from a Hover Test of a Full-Scale XV-15 Rotor," NASA TM-86833, Sept. 1985.
- [8] Bartie, K., Alexander, H., McVeigh, M., Mon, S. L., and Bishop, H., "Hover Performance Tests of Baseline Meter and Advanced Technology Blade (ATB) Rotor Systems for the XV-15 Tilt Rotor Aircraft," NASA CR-114626, Oct. 1986.
- [9] Light, J. S., "Results from an XV-15 Rotor Test in the National Full-Scale Aerodynamics Complex," *Proceedings of the 53rd American Helicopter Society Annual Forum*, AHS, Virginia Beach, Virginia, 1997.
- [10] Betzina, M. D., "Rotor Performance of an Isolated Full-Scale XV-15 Tiltrotor in Helicopter Mode," *Proceedings of the American Helicopter Society Aerodynamics, Acoustics, and Test and Evaluation Technical Specialist Meeting*, AHS, San Francisco, CA, 2002, pp. 1–12.
- [11] Wadcock, A. J., Yamauchi, G. K., and Driver, D. M., "Skin Friction Measurements on a Hovering Full-Scale Tilt Rotor," *Journal American Helicopter Society*, Vol. 99, No. 4, 1999, pp. 312–319.
- [12] Kaul, U. K. and Ahmad, J., "Skin Friction Predictions Over a Hovering Tilt-Rotor Blade Using OVERFLOW2," *Proceedings of the 29th Applied Aerodynamics Conference*, AIAA, Honolulu, Hawaii, 2011, pp. 1–19.
- [13] Kaul, U. K., "Effect of Inflow Boundary Conditions on Hovering Tilt-Rotor Flows," *Proceedings of the Seventh International Conference on Computational Fluid Dynamics*, ICCFD7, Big Island, Hawaii, 2012, pp. 1–19.
- [14] Spalart, P. R. and Allmaras, S., "A One-Equation Turbulence Model for Aerodynamic Flows," *La Recherche Aéronautique*, No. 1, 1994, pp. 5–21.
- [15] Yoon, S., Pulliam, T. H., and Chaderjian, N. M., "Simulations of XV-15 Rotor Flows in Hover Using OVERFLOW," *Proceedings of the Fifth Decennial AHS Aeromechanics Specialists*, AHS, San Francisco, CA, 2014, pp. 1–11.
- [16] Sheng, C. and Zhao, Q., "Investigations of XV-15 Rotor Hover Performance and Flow Field Using U2NCLE and HELIOS Codes," *Proceedings of the Fifty-Fourth Aerospace Sciences Meeting*, AIAA, San Diego, California, 2016, pp. 1–18.
- [17] Gates, S., "Aerodynamic Analysis of Tiltrotors in Hovering and Propeller Modes Using Advanced Navier-Stokes Computations," .
- [18] Abras, J. and Narducci, R., "Analysis of CFD Modeling Techniques over the MV-22 Tiltrotor," *Proceedings of the 66th Annual Forum*, AHS, Phoenix, AZ, 2010, pp. 1–11.
- [19] Lawson, S. J., Steijl, R., Woodgate, M., and Barakos, G. N., "High performance computing for challenging problems in computational

- fluid dynamics,” *Progress in Aerospace Sciences*, Vol. 52, No. 1, 2012, pp. 19–29, DOI: 10.1016/j.paerosci.2012.03.004.
- [20] Steijl, R. and Barakos, G. N., “Sliding mesh algorithm for CFD analysis of helicopter rotor-fuselage aerodynamics,” *International Journal for Numerical Methods in Fluids*, Vol. 58, No. 5, 2008, pp. 527–549, DOI: 10.1002/d.1757.
- [21] Steijl, R., Barakos, G. N., and Badcock, K., “A framework for CFD analysis of helicopter rotors in hover and forward flight,” *International Journal for Numerical Methods in Fluids*, Vol. 51, No. 8, 2006, pp. 819–847, DOI: 10.1002/d.1086.
- [22] Osher, S. and Chakravarthy, S., “Upwind schemes and boundary conditions with applications to Euler equations in general geometries,” *Journal of Computational Physics*, Vol. 50, No. 3, 1983, pp. 447–481, DOI: 10.1016/0021-9991(83)90106-7.
- [23] Roe, P. L., “Approximate Riemann Solvers, Parameter Vectors, and Difference Schemes,” *Journal of Computational Physics*, Vol. 43, No. 2, 1981, pp. 357–372, DOI: 10.1016/0021-9991(81)90128-5.
- [24] van Leer, B., “Towards the ultimate conservative difference scheme. V.A second-order sequel to Godunov’s Method,” *Journal of Computational Physics*, Vol. 32, No. 1, 1979, pp. 101–136, DOI: 10.1016/0021-9991(79)90145-1.
- [25] van Albada, G. D., van Leer, B., and Roberts, W. W., “A Comparative Study of Computational Methods in Cosmic Gas Dynamics,” *Astronomy and Astrophysics*, Vol. 108, No. 1, 1982, pp. 76–84.
- [26] Axelsson, O., *Iterative Solution Methods*, Cambridge University Press: Cambridge, MA, 1994.
- [27] Jarkowski, M., Woodgate, M., Barakos, G. N., and Rokicki, J., “Towards consistent hybrid overset mesh methods for rotorcraft CFD,” *International Journal for Numerical Methods in Fluids*, Vol. 74, No. 8, 2014, pp. 543–576, DOI: 10.1002/flid.3861.
- [28] Dehaeze, F. and Barakos, G. N., “Aeroelastic CFD Computations for Rotor Flows,” *Proceedings of the 37th European Rotorcraft Forum*, ERF, Galarate, Italy, 2011, pp. 1–20.
- [29] Jimenez, A. and Barakos, G. N., “Hover Predictions on the S-76 Rotor using HMB2,” *Proceedings of the 53rd Aerospace Sciences Meeting*, AIAA, Kissimmee, Florida, 2015, pp. 1–34.
- [30] Menter, F. R., “Two-Equation Eddy-Viscosity Turbulence Models for Engineering Applications,” *AIAA Journal*, Vol. 32, No. 8, 1994, pp. 1598–1605, DOI: 10.2514/3.12149.
- [31] Menter, F. R., Smirnov, P. E., Liu, T., and Avancha, R., “A One-Equation Local Correlation-Based Transition Model,” *Flow Turbulence Combust*, Vol. 95, No. 4, 2015, pp. 583–619, DOI:10.1007/s10494-015-9622-4.
- [32] Menter, F., Langtry, R., Rikki, R., Suzen, S., Huang, P., and Volker, S., “A Correlation-Based Transition Model Using Local Variables - Part I: Model Formulation.” *Journal of Turbomachinery*, Vol. 128, No. 3, 2006, pp. 1598–1605.
- [33] Brocklehurst, A., *High Resolution Method for the Aerodynamic Design of Helicopter Rotors*, Ph.D. thesis, University of Liverpool, UK, June 2013.
- [34] Jeong, J. and Hussain, F., “On the Identification of a Vortex,” *Journal of Fluid Mechanics*, Vol. 285, No. 1, 1995, pp. 69–94, DOI: 10.1017/S0022112095000462.
- [35] Wadcock, A. J., Yamauchi, G. K., and Driver, D. M., “Skin Friction Measurements on a Hovering Full-Scale Tilt Rotor,” *Journal of the American Helicopter Society*, Vol. 44, No. 4, 1999, pp. 321–319, DOI: <http://dx.doi.org/10.4050/JAHS.44.312>.
- [36] Acree, C., “Rotor Design Options for Improving XV-15 Whirl-Flutter Stability Margins,” NASA TP–2004-212262, March 2004.

Table 1: Radial location of the XV-15 rotor blade aerofoils [7].

$r/R$	Aerofoil
0.09	NACA 64-935
0.17	NACA 64-528
0.51	NACA 64-118
0.80	NACA 64-(1.5)12
1.00	NACA 64-208

Table 2: Geometric properties of the full-scale XV-15 rotor [10].

Parameter	Value
Number of blades, $N_b$	3
Rotor radius, $R$	150 inches
Reference blade chord, $c_{ref}$	14 inches
Aspect ratio, $R/c_{ref}$	10.71
Rotor solidity, $\sigma$	0.089
Linear twist angle, $\Theta$	$-40.25^\circ$

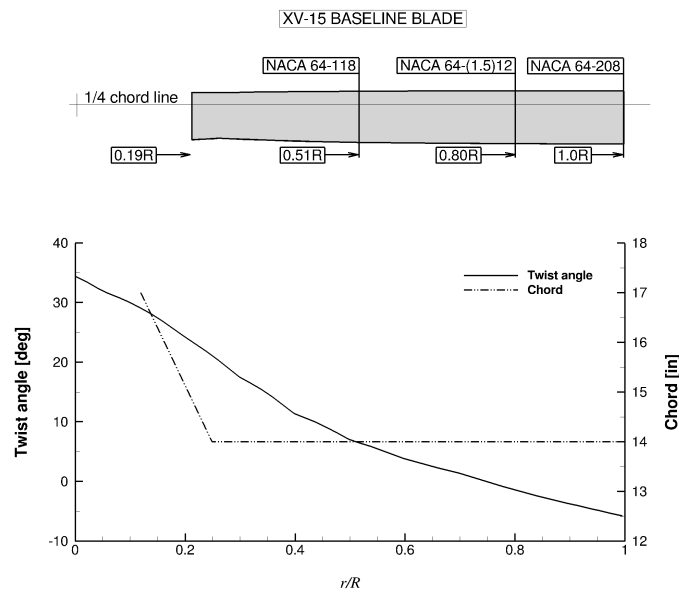


Figure 1: Planform of the XV-15 rotor blade (above) and twist and chord distributions [36] (below).

Table 3: Meshing parameters for the XV-15 rotor mesh.

	Coarse Mesh	Medium Mesh
Background mesh size (cells)	2.6 million	6.0 million
Blade mesh size (cells)	3.6 million	3.6 million
Overall mesh size (cells)	6.2 million	9.6 million
Height of the first mesh layer at blade surface	$1.0 \cdot 10^{-5} c_{ref}$	$1.0 \cdot 10^{-5} c_{ref}$

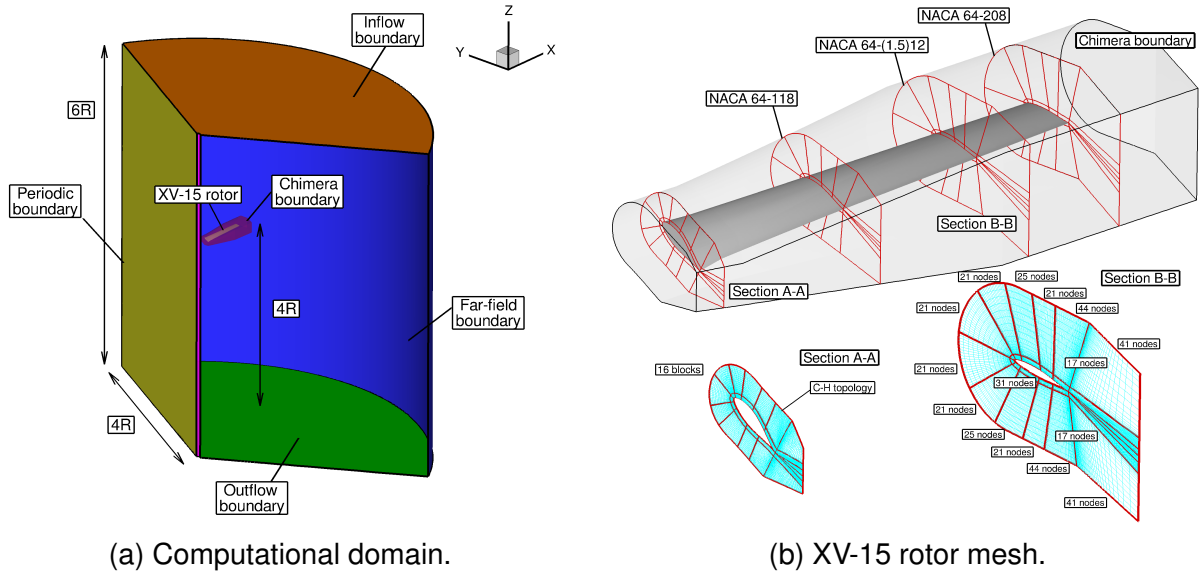


Figure 2: Computational domain and boundary conditions employed (left) and detailed view of the XV-15 rotor mesh (right).

Table 4: Flow conditions for the full-scale XV-15 tiltrotor blade.

	Helicopter Mode	Aeroplane Mode
Blade-tip Mach number ( $M_{tip}$ )	0.69	0.54
Reynolds number ( $Re$ )	$4.95 \cdot 10^6$	$4.50 \cdot 10^6$
Blade pitch angle ( $\theta_{75}$ )	$3^\circ, 5^\circ, 10^\circ, 13^\circ$	$26^\circ, 27^\circ, 28^\circ, 28.8^\circ$
Grid	Coarse and Medium	Coarse and Medium
Turbulence model	$k - \omega$ SST	$k - \omega$ SST

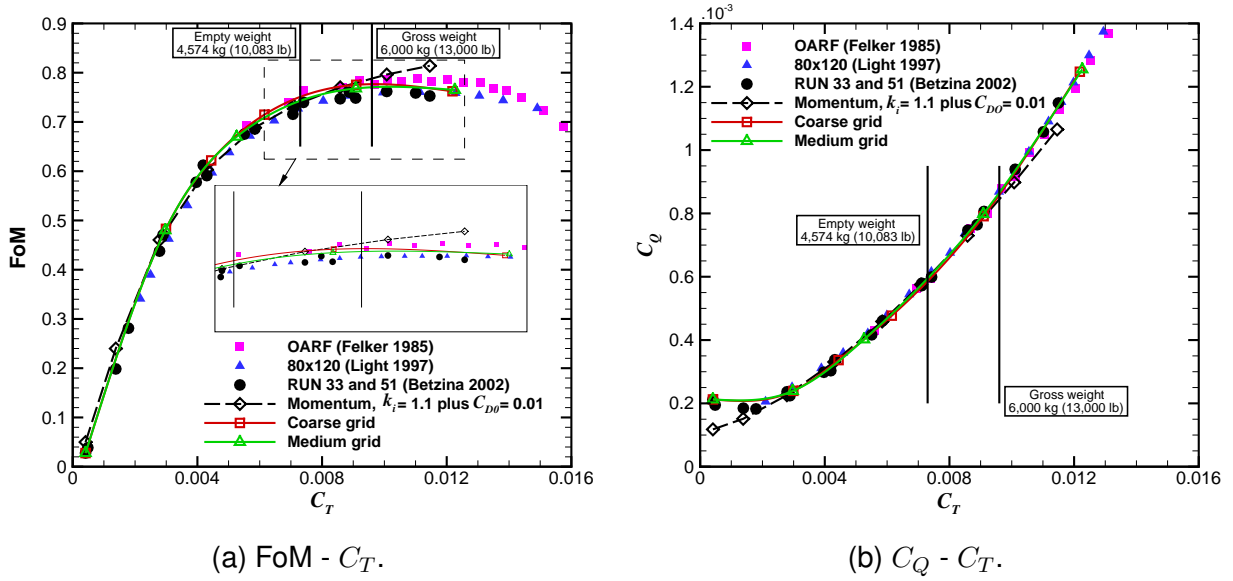


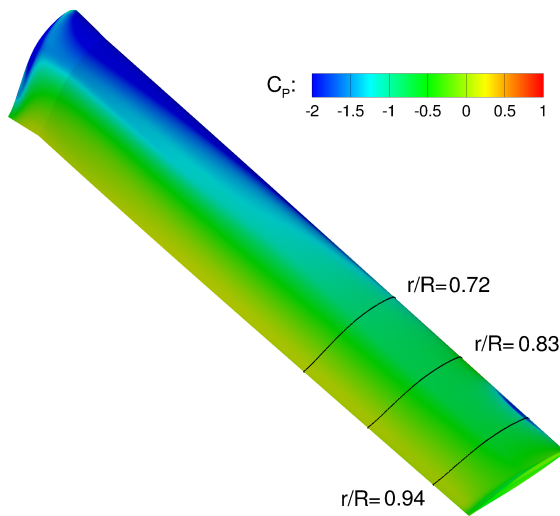
Figure 3: Effect of the mesh density on the figure of merit (left) and torque coefficient (right) for the full-scale XV-15 rotor.

Table 5: Predicted and experimental peak FoM for the full-scale XV-15 rotor.

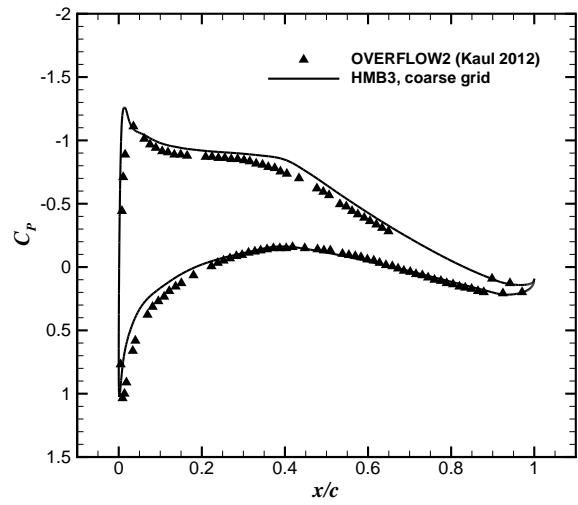
	Experiments			CFD	
	Felker [7]	Light [9]	Betzina [10]	Coarse grid	Medium grid
FoM	0.788	0.761	0.761	0.776	0.768

Table 6: Predicted and experimental [11] figure of merit at collective pitch angle of  $10^\circ$ .

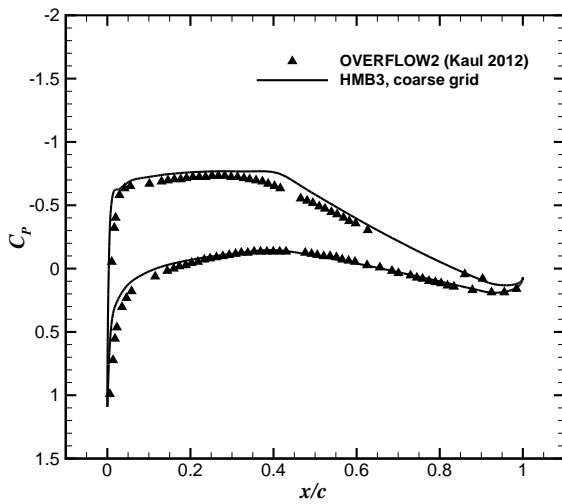
Case	FoM	Difference [%]
Coarse grid	0.775	1.97%
Medium grid	0.768	1.05%
Experiment	(0.760) [15]	-



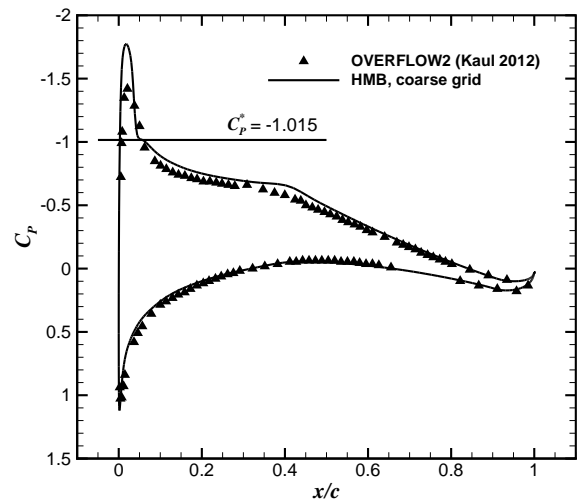
(a) Surface pressure coefficient.



(b)  $r/R = 0.72$ .

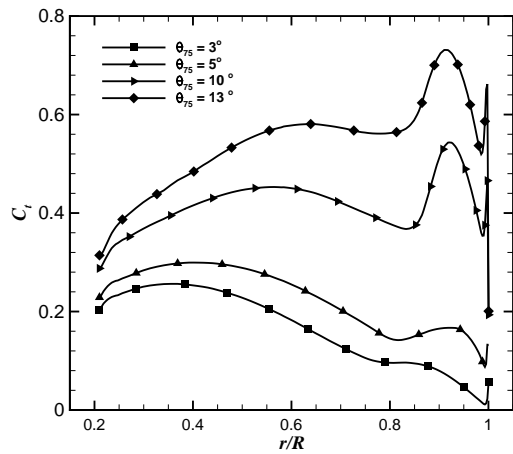


(c)  $r/R = 0.83$ .

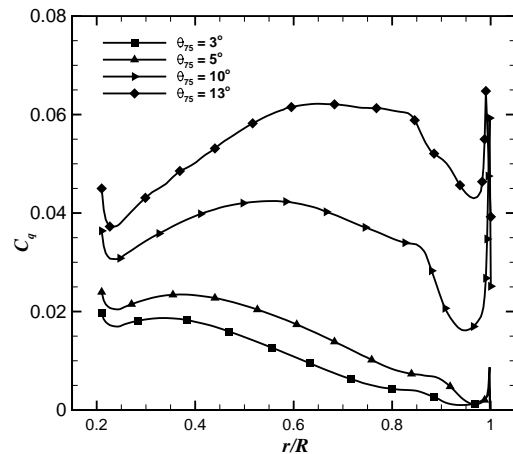


(d)  $r/R = 0.94$ .

Figure 4: Comparison of predicted surface pressure coefficient between HMB3 using the coarse grid and OVERFLOW2 from Kaul *et al.* [13].

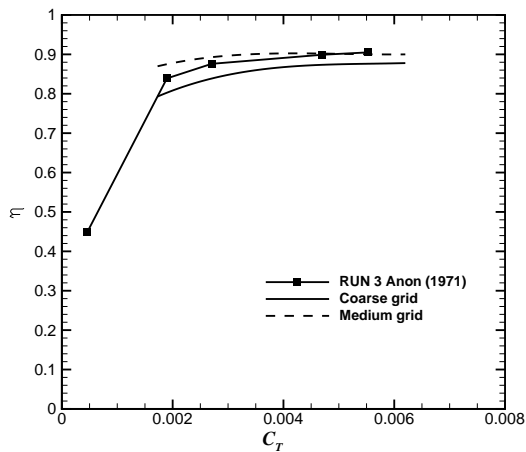


(a) Thrust coefficient.

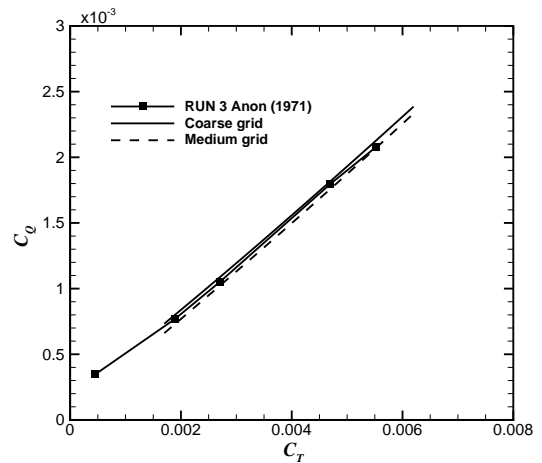


(b) Torque coefficient.

Figure 5: Blade section thrust coefficient (left) and torque coefficient (right) for the full-scale XV-15 rotor in helicopter mode.

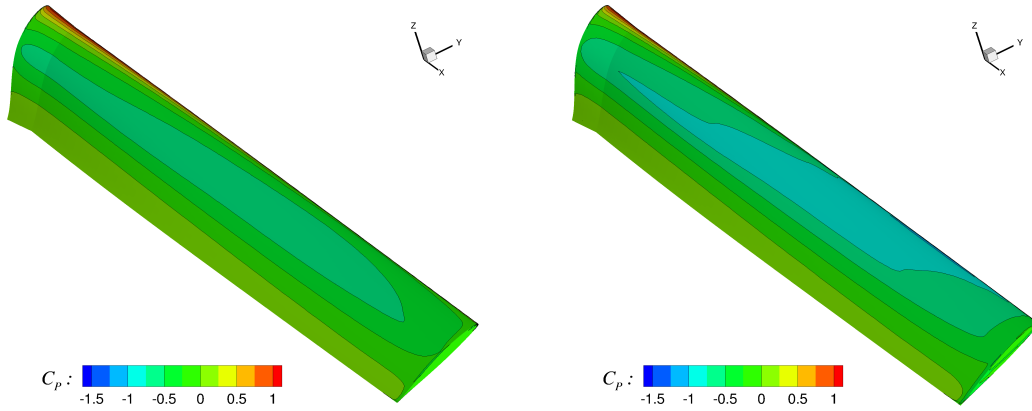


(a) Propeller propulsive efficiency - Thrust coefficient.



(b) Torque coefficient - Thrust coefficient.

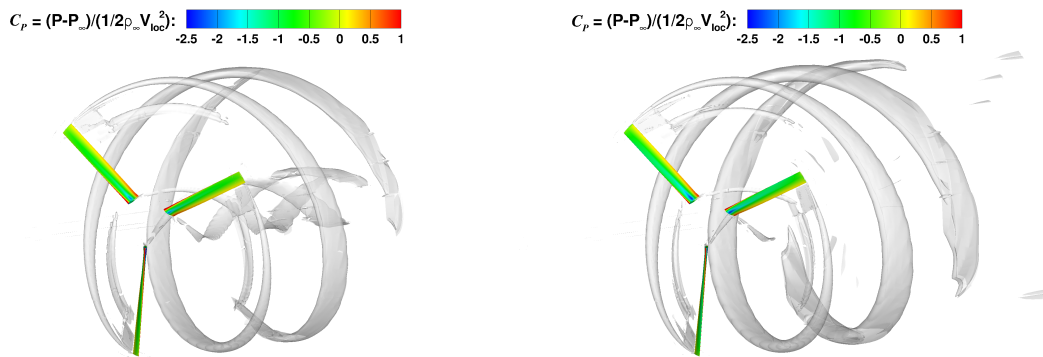
Figure 6: Propulsive propeller efficiency and torque coefficient as function of the thrust coefficient for the XV-15 rotor blade in propeller mode configuration.



(a) Blade pitch angle  $\theta_{75} = 26^\circ$ .

(b) Blade pitch angle  $\theta_{75} = 28.8^\circ$ .

Figure 7: Contours of surface pressure coefficient for the XV-15 rotor blade.



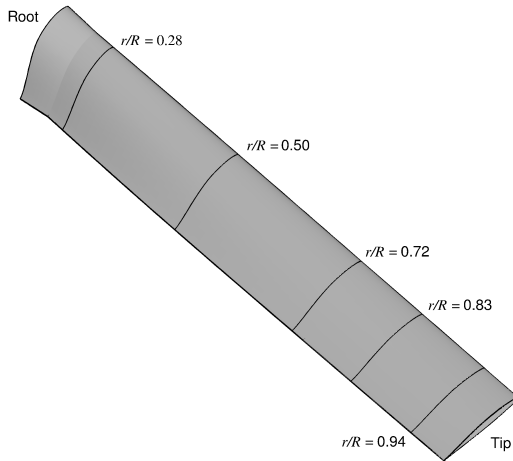
(a) Blade pitch angle  $\theta_{75} = 26^\circ$ .

(b) Blade pitch angle  $\theta_{75} = 28.8^\circ$ .

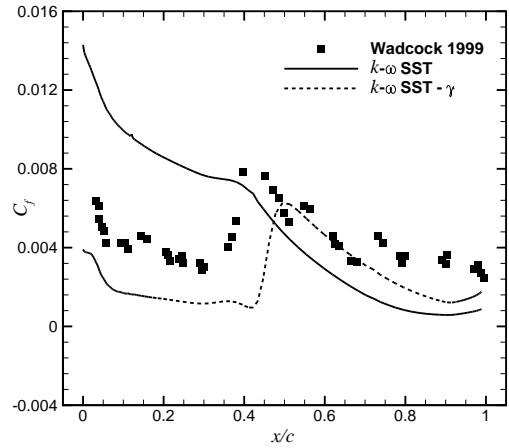
Figure 8: Wake visualisation of the propeller wake using  $Q$ -criterion shaded by contours of  $C_P$  at blade pitch angle of  $\theta_{75} = 26^\circ$  (left) and  $\theta_{75} = 28.8^\circ$  (right).

	$C_T$	$C_Q$	FoM
FT $3^\circ$	0.00293	0.000249	0.450
TM $3^\circ$	0.00297	0.000223	0.512
FT $10^\circ$	0.00906	0.000807	0.756
TM $10^\circ$	0.00909	0.000803	0.763

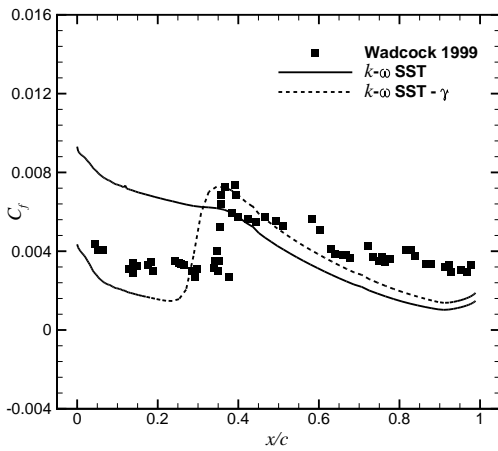
Table 7: Comparison of predicted  $C_T$ ,  $C_Q$ , and FoM at  $3^\circ$  and  $10^\circ$  collective angles between the fully-turbulent  $k - \omega$  SST and transitional model  $k - \omega$  SST- $\gamma$ . Conditions employed:  $M_{tip} = 0.69$  and  $Re = 4.95 \cdot 10^6$ . FT=Fully-Turbulent; TM=Transitional-Model.



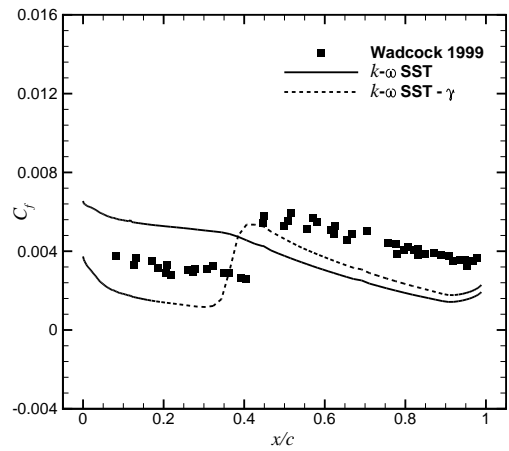
(a) Radial stations.



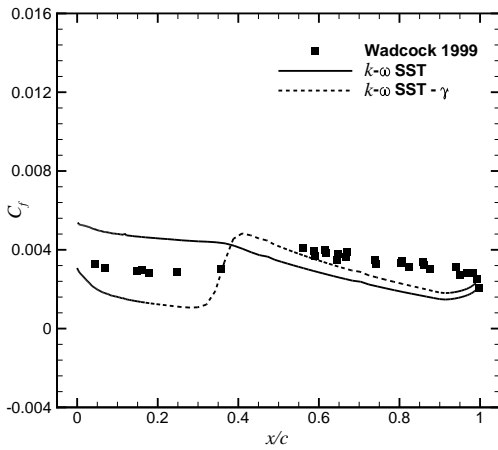
(b)  $r/R = 0.28$ .



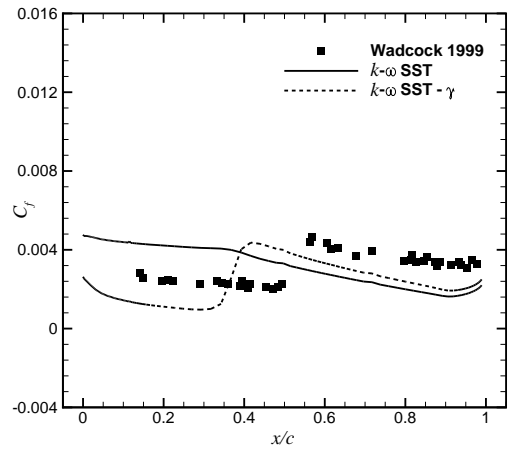
(c)  $r/R = 0.50$ .



(d)  $r/R = 0.72$ .

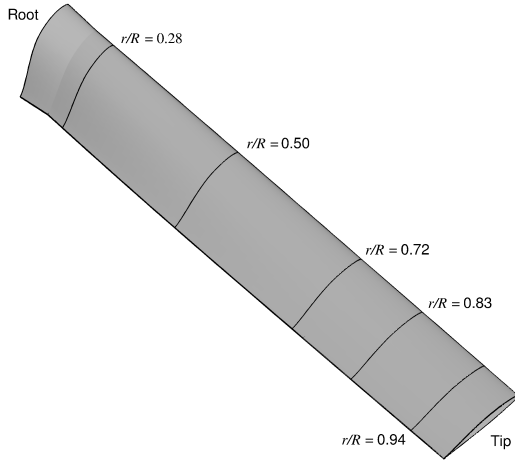


(e)  $r/R = 0.83$ .

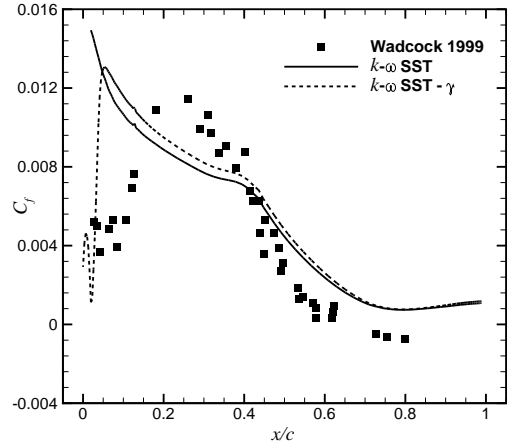


(f)  $r/R = 0.94$ .

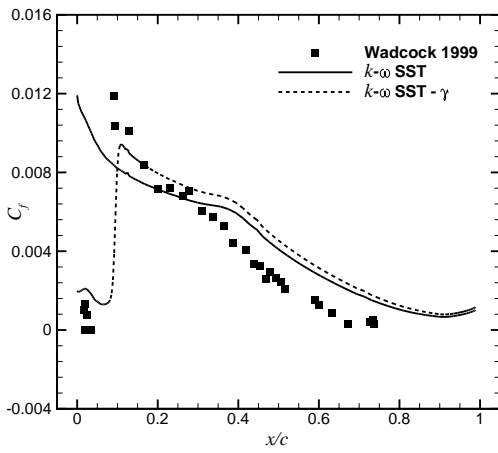
Figure 9: Comparison between the computed skin friction coefficient using a fully turbulent and transitional model solutions with the experimental data of Wadcock *et al.* [35]. Conditions employed:  $M_{\text{tip}} = 0.69$ ,  $Re = 4.95 \cdot 10^6$ , and  $\theta_{75} = 3^\circ$ .



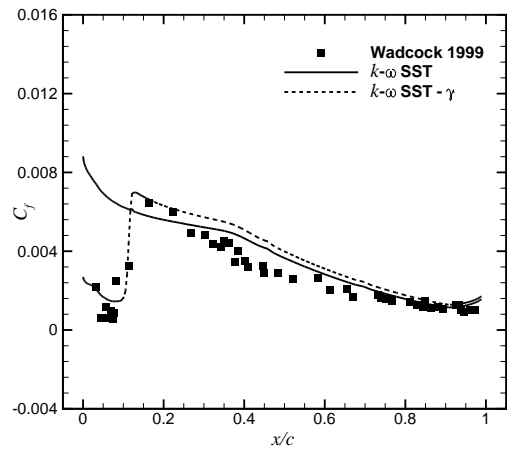
(a) Radial stations.



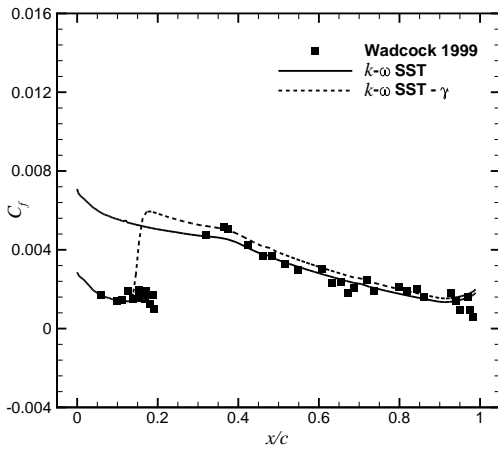
(b)  $r/R = 0.28$ .



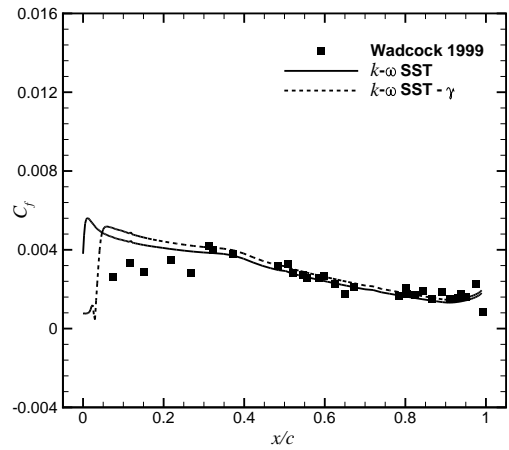
(c)  $r/R = 0.50$ .



(d)  $r/R = 0.72$ .

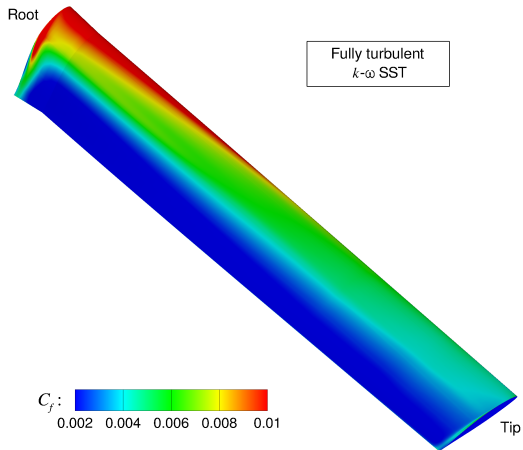


(e)  $r/R = 0.83$ .

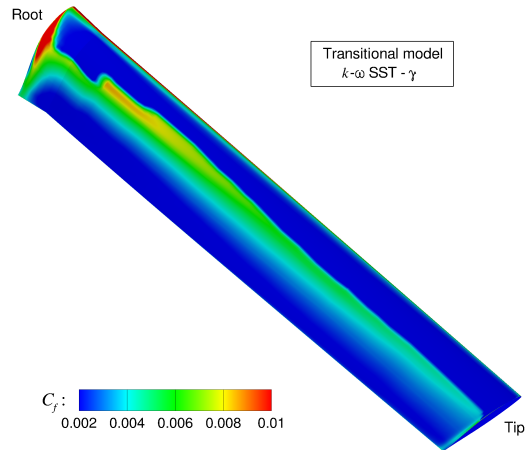


(f)  $r/R = 0.94$ .

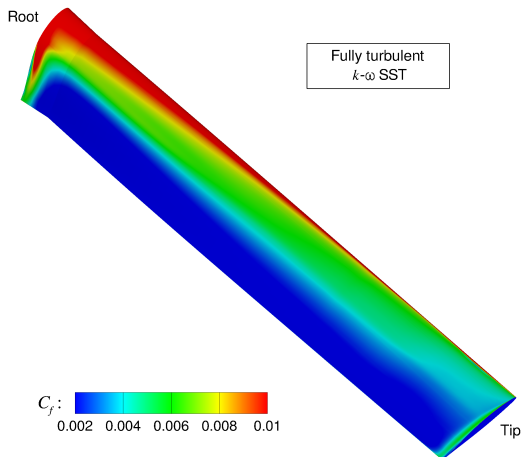
Figure 10: Comparison between the computed skin friction coefficient using a fully turbulent and transitional model solutions with the experimental data of Wadcock *et al.* [35]. Conditions employed:  $M_{tip} = 0.69$ ,  $Re = 4.95 \cdot 10^6$ , and  $\theta_{75} = 10^\circ$ .



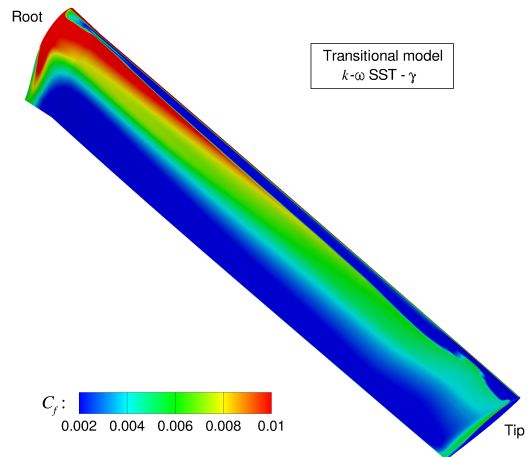
(a) Fully turbulent solution,  $\theta_{75} = 3^\circ$ .



(b) Transitional model solution,  $\theta_{75} = 3^\circ$ .



(c) Fully turbulent solution,  $\theta_{75} = 10^\circ$ .



(d) Transitional model solution,  $\theta_{75} = 10^\circ$ .

Figure 11: Surface skin friction coefficient for the fully turbulent and transitional model cases.